Interface Chemistry, Band Alignment, and Thermal Stability Study of Sn Metal Contact on Bulk and Monolayer MoS$_2$

Joy Roy [1] Seong Yeoul Kim [1] and Robert M. Wallace [1,a]

[1]Department of Materials Science and Engineering, The University of Texas at Dallas, Richardson, TX 75080, United States of America

[a] Electronic mail: rmwallace@utdallas.edu

Two-dimensional semiconductors such as transition metal dichalcogenides are making impressive strides in a short duration compared to other candidates. However, to unlock their full potential for advanced logic transistors, attention must be given to improving the contacts or interfaces they form. One approach is to interface with a suitable low work function metal contact to allow the surface Fermi level (E_F) movement towards intended directions, thereby augmenting the overall electrical performance. In this work, we implement physical characterization to understand the Tin (Sn) contact interface on monolayer and bulk molybdenum disulfide (MoS$_2$) via in-situ X-ray photoelectron spectroscopy (XPS) and ex-situ atomic force microscopy (AFM). A Sn contact exhibited a van der Waals (vdW) type weak interaction with the MoS$_2$ bulk surface where no reaction between Sn and MoS$_2$ is detected. In contrast, reaction products with Sn-S bonding is detected with a monolayer surface consistent with a covalent-like interface. Band alignment at the interface indicates that the Sn deposition induces n-type properties in the bulk substrate, while the E_F of the monolayer remains pinned. In addition, the thermal stability of Sn on the same substrates is investigated in a sequential ultra-high vacuum (UHV) annealing treatment at 100, 200, 300, and 400º C. Sn sublimated/desorbed from

both substrates with increasing temperature, which is more prominent on the bulk substrate after annealing at 400°C. Additionally, Sn significantly reduced the monolayer substrate and produced detectable interface reaction products at higher annealing temperatures. The findings can be strategized to resolve challenges with contact resistance that the device community is having with TMDs.

I. INTRODUCTION

To allow continuous device scaling with enhancing mobility and without performance variability, 2D Transition metal dichalcogenides (TMDs) can be a desirable replacement for Si in near future for advanced field effect transistors (FETs).[1,2] Numerous research studies are underway to make the TMDs commercially feasible for modern-day digital electronics. Whether chemical vapor deposition (CVD) grown or mechanically exfoliated for research purposes, MoS_2 has attracted significant interest for decades being highly suitable for electronic and optoelectronic applications due to its sizable band gap and chemical stability.[3–5] With a near-ideal passivated surface, MoS_2 can be scaled down to atomically thin thicknesses without degradation of mobility.[6,7] This inherent 2D nature and enhanced functionality provided by MoS_2 allows hetero-integration at the back-end-of-line (BEOL) processing for integrated circuit technology.[8,9] Whereas Si technology has its limitations, two fundamental challenges most TMD semiconductors confront are surface defects and the highly resistive Schottky contact interface they

1   establish with metals. Since conventional doping can induce defects and is difficult to

2   control, metal contacts are more suitable for realizing the desired doping polarity.[10] Low

3   contact resistance with near ohmic behavior ensures efficient carrier injection to the

4   channel material. Metals with reasonably low work functions that align with or close to

5   the conduction band of n-type TMDs have demonstrated the potential to address this

6   contact resistance issue.[11,12]

7   The work function (Φ) is a crucial surface property of contact metals that implies

8   the minimum energy required for charge emission from the metal surface to a point in

9   vacuum immediately outside the surface.[13] Essentially, Φ affects the Schottky barrier

10   height when a contact interface between a metal and semiconductor forms. Though

11   tuning the Schottky barrier height by Φ at the metal-TMD interface can be hindered by

12   various types of intrinsic defects, recent works using Sn, In, Bi, and Sb (low Φ)

13   successfully improved the contact resistance by minimizing the barrier height and

14   forming an Ohmic like contact.[14–16] Chou et al. reported that Au capped Sn (contact)

15   remelting step achieves a conformal contact interface with monolayer MoS_2 and leads to

16   high current linearity at small V_{DS} (drain-source voltage) in their short channel n-type

17   FETs.[5] Another study by Kumar et al. using Sn and In with Au capping lowered the

18   contact resistance on monolayer MoS_2, achieving an $R_c \sim 200$ Ω-μm. Their statistical

19   analysis (~700 transistors) of the transistor performance found the contacts were stable up

20   to 250 ˚C, above which they turn to an alloy with Au and can be stable at temperatures as

21   high as 450 ˚C.[14] In addition, the ultraclean van der Waals contact interface using In (low

22   Φ) has achieved a free adjustable barrier height with various TMD-based 2D

23   semiconductors.[17] These prior studies demonstrate significant enhancements in contact

1 properties using these recently prevalent low Φ metals. However, they lack a systematic

2 understanding of the interfacial chemistry at the metal-TMD interface, as well as certain

3 band alignments, which play a major role in determining device performance variability.

4   In this work, we examined the correlation between the Sn contact interface with

5 bulk and monolayer MoS_2 substrates and their respective contact properties. Interfacial

6 chemistry and band alignments were obtained analytically and compared with pre-

7 metallization states for a fundamental understating of contact interface chemistry. In

8 addition, to understand the robustness and compatibility of the BEOL processing

9 conditions, the thermal stability of the Sn contact on MoS_2 substrates was studied under

10 the UHV environment.

11

II. EXPERIMENTAL

13   Bulk crystals used in this work were purchased from HQ Graphene.[18] The 1L-

14 MoS_2 film sample was cleaved into pieces from a wafer grown by 2DLayer.[19] The

15 growth technique involves CVD of 1L-MoS_2 film on a 90 nm SiO_2/Si wafer substrate

16 with complete coverage of the 50 mm wafer. Exfoliated MoS_2 bulk crystals and the as-

17 received 1L-MoS_2 films were attached on a 4 inches stainless steel (SS) plate using SS

18 screws for surface analysis. Within a brief atmospheric exposure of around 30 seconds

19 after ex-situ exfoliation of a bulk MoS_2 crystal, the samples were loaded into the load

20 lock of the cluster system, a schematic diagram with process flow is available in the

21 supplementary material. In this work, approximately 1 nm of Sn metal was deposited on

22 freshly exfoliated bulk-MoS_2 and 1L-MoS_2 via a physical vapor deposition technique

23 using an electron beam under UHV (deposition chamber base pressure 2×10^{-11} mbar)

1   condition at room temperature. During metallization, polymer-assisted transfer or any

2   other processing steps, such as lithography, were avoided to prevent potential alterations

3   in the interface chemistry due to contaminants. After metallization, one set of samples

4   was unloaded to observe the changes in the morphology of the surfaces, and another set

5   went through sequential post-metallization annealing with in-situ characterization in

6   between steps. Samples were heated through indirect resistive heating under UHV

7   conditions at 100, 200, 300, and 400° C for 1 hour. The anneal temperature was ramped

8   up and cooled down in ~1 hour enabling very low outgassing and a chamber pressure

9   below 5×10^{-9} mbar. The heater temperature reading is calibrated using Si and Ge wafers

10   on an SS plate with an error margin of $\pm 10\ ^\circ$C. For spectrum comparison studies, a

11   reference Sn thick film (~ 70 nm) was deposited on a Si/SiO_2 wafer under UHV

12   conditions.

13   For characterization, XPS analysis on sample surfaces was conducted using a

14   monochromatic Al Kα source and an Omicron EA125 hemispherical analyzer, achieving

15   a resolution of ± 0.05 eV. Initially, samples were characterized in their as-exfoliated or

16   loaded condition (control sample) before metal deposition. After UHV electron beam

17   metal depositions, the samples were transferred to the analytical chamber under UHV

18   conditions (3×10^{-11} mbar) via the transfer tube for *in-situ* characterization. XPS spectra

19   after metallization were compared to the freshly exfoliated surfaces. E_F shifts due to

20   metal deposition were extracted from the core level shifts.[20] Subsequently, further XPS

21   analysis was done after each annealing step maintaining the in-situ conditions. In addition

22   to XPS, AFM was used ex-situ to characterize the surface morphology of MoS_2 bulk

23   crystals and 1L-MoS_2 films. For this purpose, an Oxford Asylum Research Jupiter XF

1   AFM tool was used in non-contact tapping mode in the cleanroom facility. The AFM

2   analysis was done initially before loading the sample, then one set after metallization and

3   another after 400^0 C annealing. Aanalyzer software[21] was used for XPS analysis and

4   Gwyddion 2.60 software[22] was used for measuring RMS (root mean square) roughness

5   from AFM data.

6

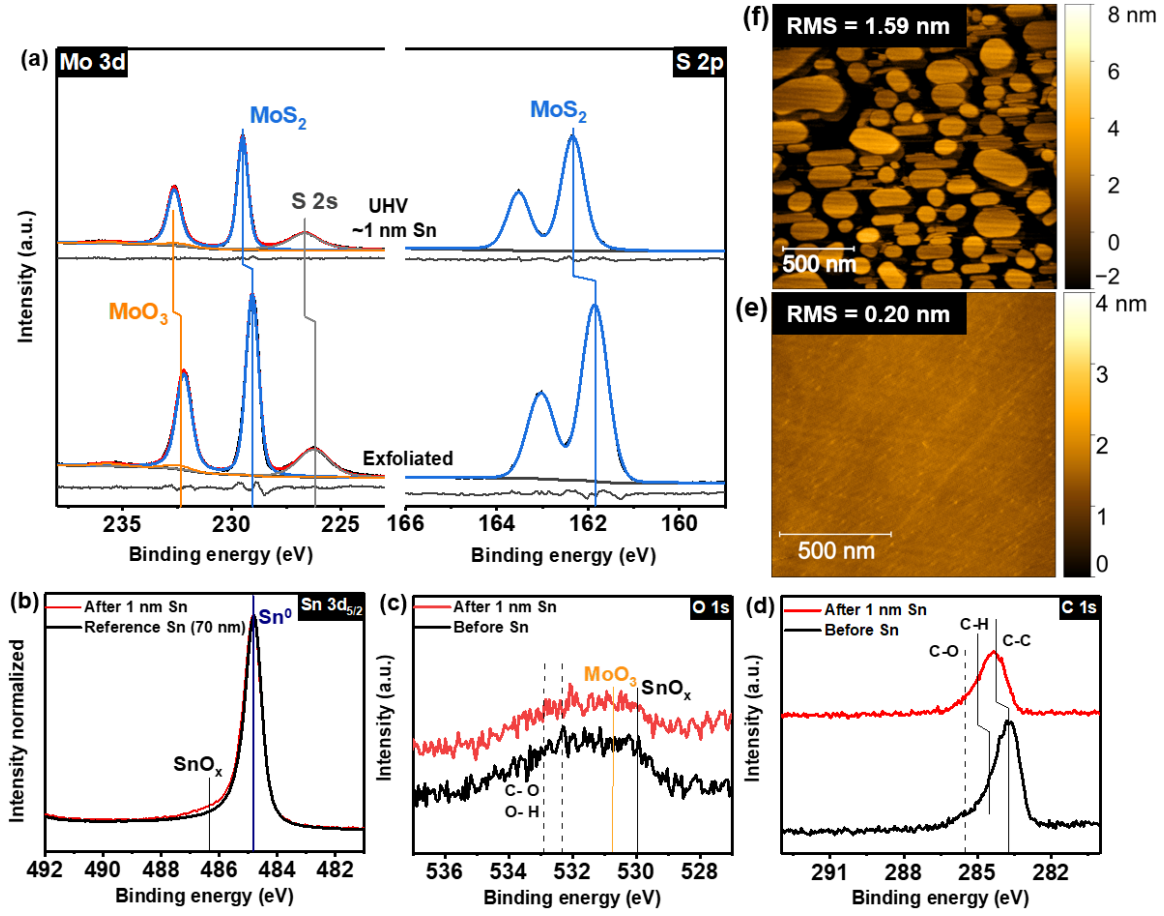### 7   III. RESULTS AND DISCUSSION

8   *A.   Interface chemistry*

9   *1.   Sn contacts on bulk MoS$_2$*

10   Figure 1 shows XPS results of Sn/ MoS$_2$ bulk crystal surfaces/interfaces before

11   and after Sn deposition under UHV conditions. The initial (exfoliated) binding energy

12   (BE) position for Mo $3d$ and S $2p$ are found at 229.05 and 161.85 eV respectively,

13   attributed to the MoS$_2$ chemical bonding state[23] (Figure 1 (a)). The interface reaction after

14   Sn deposition is below the detection limit of XPS for Sn/MoS$_2$ bulk interface. The

15   formation of MoS$_2$ is thermodynamically favorable since the Gibbs free energy $\Delta G°_{f, MoS2}$

16   (-112.95 kJ/mol) is more negative relative to Sn-S bond formation ($\Delta G°_{f, SnS}$ = -98.3

17   kJ/mol).[24] Moreover, a reaction between Sn and Mo in MoS$_2$ or forming an intermetallic

18   alloy is unlikely at room temperature in UHV conditions.[25,26] The absence of an

19   additional chemical state in Mo $3d$ and S $2p$ core levels after metallization under UHV

20   condition indicates the formation of a vdW bonding interface between Sn and MoS$_2$ bulk.

21   The full widths at half-maximum (FWHM) of the MoS$_2$ state in the Mo $3d$ (0.59 $\pm$ 0.05

22   eV) core levels stay almost the same before and after Sn depositions under UHV

23   conditions and indicate that the interface reaction of Sn and MoS$_2$ bulk is below the limit

1   of detection. The intensity of core levels (Mo $3d$ and S $2p$) spectra decreased due to the

2   Sn metal layer on top of MoS_2.

3   Even though a Sn film does not result in detectible reaction products with the

4   MoS_2 bulk, the shifts of the MoS_2 state in Mo $3d$ and S $2p$ spectra following Sn

5   deposition show the change in the electronic property of the substrate. This shift of ~0.45

6   eV impacts the band alignment and barrier height at the Sn/bulk MoS_2 interface. The

7   shifts in the core level spectra and relevant discussions are displayed in the

8   supplementary material and the band alignment section. A small amount of oxidation of

9   the MoS_2 bulk surface detected before metal deposition might result from short air

10   exposure after exfoliation. The oxidation of MoS_2 bulk in the air is thermodynamically

11   favorable as

1

2

FIG. 1. (a) Mo 3d and S 2p, (b) Sn 3 $d5/2$, (c) O 1s and (d) C 1s spectra of bulk MoS$_2$

sample before and after Sn depositions under UHV condition, (e) Ex-situ AFM images of

MoS$_2$ bulk crystal surface after exfoliation and (f) after Sn deposition in UHV conditions

showing root mean square (RMS) roughness in nm unit. The gray plot below the spectral

data in (a) is the peak fit residual.

$\Delta G\degree_{f, MoO2}$ = -266.50 kJ/mol and $\Delta G\degree_{f, MoO3}$ = -222.70 kJ/mol. Some studies have

highlighted slow oxidation is possible for MoS$_2$ in ambient conditions which prefers

MoO$_3$.[27] In addition, S vacancies can induce MoS$_2$ surface oxidation.[28] In our sample, the

BE position suggests this type of oxidation prior to metallization. After contact interface

formation, a small concentration (<0.5 atom%) of SnO$_x$ has been detected on the higher

1   BE shoulder of Sn $3d$ and lower BE tail of O $1s$ spectra (Figures 1(b) and 1(c)). Such

2   SnO_x formation is consistent with thermodynamic values for $\Delta G°_{f, SnO}$ = -251.90 kJ/mol,

3   and $\Delta G°_{f, SnO2}$ = -515.8 kJ/mol.[24] In addition, the interdiffusion between Sn-MoO_3

4   resulting from the interaction at the interface may have a small contribution to the

5   oxidation process.[29] Adventitious carbon bonds (C-C, C=O, and C-O) in the bulk MoS_2

6   spectrum (Figure 1 (d)) are probably from the ex-situ transfer process. However, no

7   carbon reaction products are detected at lower binding energy (metal carbide~282 eV).[30]

8   This indicates that carbon's reaction with Sn and MoS_2 bulk is below the detection limit

9   of XPS.

10   From AFM analysis after UHV metal depositions, Sn elliptical and circular islands

11   are observed. (Figures 1 (e) and (f)) These island formation characteristics infer that the

12   interface reaction between Sn and MoS_2 bulk is not favored. This observation is consistent

13   with both thermodynamic Gibbs free energy[24] and XPS analysis. Thus, a vdW gap contact

14   is expected at the Sn/ MoS_2 bulk interfaces for UHV deposition of Sn. The detection of Sn

15   islands on MoS_2 bulk in this work aligns with the observation of Volmer-Weber growth of

16   Ag metal film deposited similarly through physical vapor deposition on bulk MoS_2 flakes

17   under UHV conditions.[31]

18   *2.   Sn contacts on 1-L MoS₂*

19   Unlike MoS_2 bulk systems, there is a notable difference for 1-L MoS_2. Interface

20   reactions are observed after Sn deposition. A slight reduction of MoS_2 is also detected at

21   Sn/1L-MoS_2 film interfaces deposited under UHV condition as shown in Figure 2 (a).

22   The presence of the MoS_x (sub-stoichiometric, x < 2) state in the Mo $3d$ spectra and an

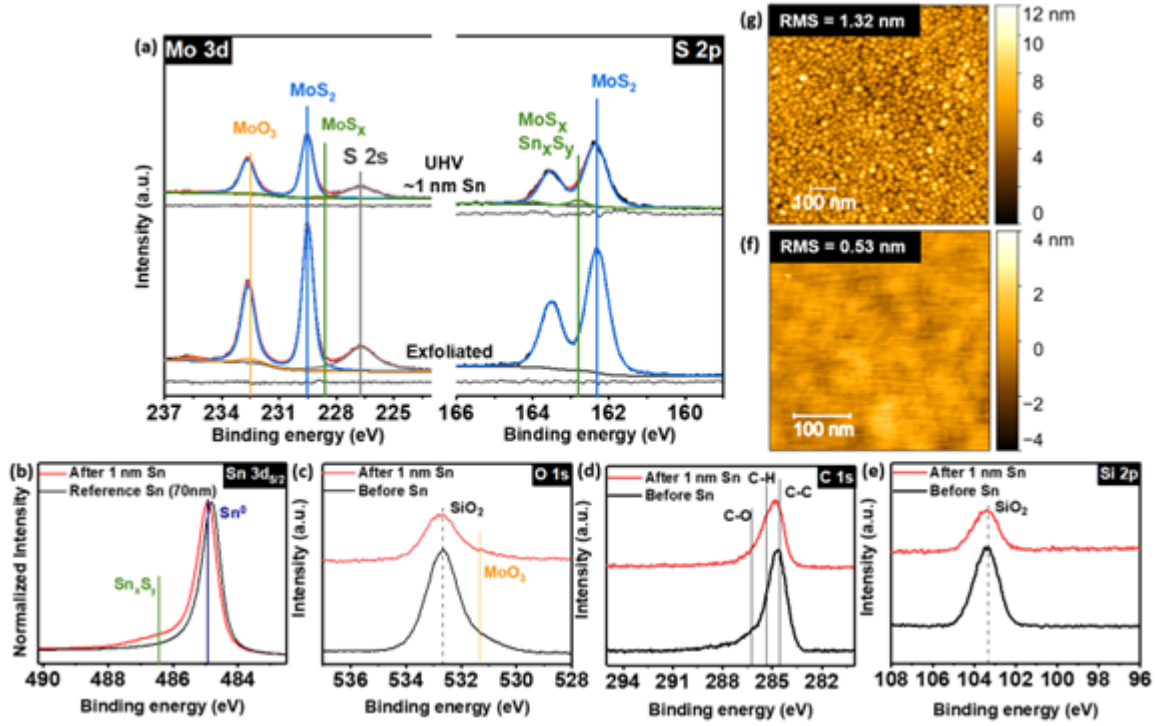23   additional Sn_xS_y/MoS_x state in the S $2p$ spectra, indicates a reaction occurring at the

1 metal/semiconductor interface. Since only a sub-stochiometric state between Sn and S is

2 detected in Sn $3d$ and S $2p$ spectra, we will use Sn_xS_y to denote the reaction product in the

3 rest of the discussion of the Sn/1-L MoS$_2$ interface.

4   Under UHV conditions, there have been reports of a reduction reaction occurring

5 in the Ni/ MoS$_2$ bulk system that is analogous to the aforementioned reaction

6 mechanism.[31] Though, reactions between Sn and MoS$_2$ at room temperature are not

7 thermodynamically favorable,[24] charge transfer between Sn and MoS$_2$ bulk induced by

8 the intrinsic defects of 1-L MoS$_2$ (like S vacancies)[32] could shift the $\Delta G°_{f,SnS}$ more

9 negative than that of MoS$_2$. This Sn reduction reaction observed only in Sn/1L- MoS$_2$

10 film systems indicates that the Sn metal contact reaction with MoS$_2$ is not inherent and

11 varies significantly with the surface defect density (CVD grown 1-L MoS$_2$). In addition,

12 core levels of Mo $3d$ and S $2p$ didn't shift after metallization. This kind of behavior is

13 attributed to E$_F$ pinning, most probably caused by surface defect states.

14   The (slight) oxidation of the 1L- MoS$_2$ film (figures 2 (a) and (c)) is rational due

15 to the air exposure during the ex-situ loading process.[27,28] The intensities of oxide states

16 in Mo $3d$ decreased after Sn deposition under UHV conditions. This is likely due to the

17 metal deposition causing the overall lowering of core level intensities of 1-L MoS$_2$

18 substrate. Carbon and oxygen reactions with Sn are below the detection limit of XPS

19 after Sn deposition as shown in Figures 2 (b-d). The absence of any additional metal

20 silicide chemical states in the Si $2p$ spectra (Figure 2 (e)) indicates that the reaction

21 between Sn and SiO$_2$ substrate of 1L- MoS$_2$ film is also below the detection limit of XPS.

22   An increased surface roughness is detected by ex-situ AFM analysis after Sn

23 depositions on 1L- MoS$_2$ films under UHV conditions as shown in Figures 2 (f) and (g).

1

2

FIG. 2. (a) Mo $3d$ and S $2p$, (b) Sn $3d_{5/2}$, (c) O $1s$, (d) C $1s$, and (e) Si $2p$ core level
spectra of 1L MoS$_2$ sample before and after Sn depositions under UHV condition, (f) Ex-
situ AFM images of the monolayer crystal surface and (g) after Sn deposition in UHV
conditions showing root mean square (RMS) roughness in nm unit. The gray plot below
the spectral data in (a) is the peak fit residual.

8

9   Sn islands or clusters are significantly smaller and well-connected in this case compared

10   to the bulk MoS$_2$ substrate (Figure 1 (f)). Since sub-stoichiometric MoS$_x$ and Sn$_x$S$_y$

11   bonding states are detected at the Sn/1L- MoS$_2$ interface in XPS analysis, greater

12   interaction (covalent bonding) between Sn and the monolayer surface is facilitated. As

13   noted in the AFM image results, this enhanced interaction leads to a layer-by-layer

14   growth morphology instead of forming larger islands. Moreover, the surface morphology

15   of 1L- MoS$_2$ prior to deposition is more uneven compared to bulk crystal which suggests
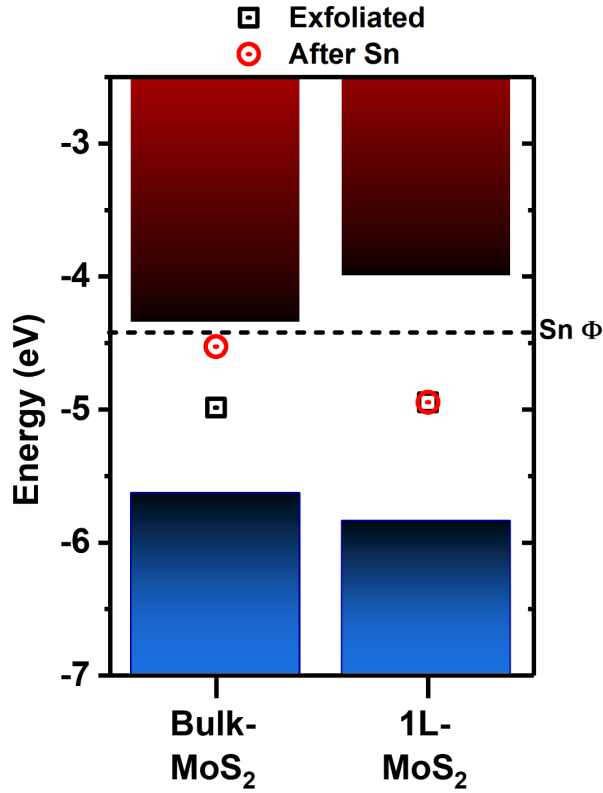
1 that nonuniform growth of MoS_2 layer on Si/SiO_2 substrate occurs. Taken together, the

2 results suggest that it is reasonable to attribute the clusters in AFM images to the mixture

3 of mostly Sn metal and some Sn/ MoS_2 reaction products. This finding is consistent with

4 the theory that defects (grain boundaries, S vacancies) may facilitate reactions between

5 metals and TMDs, since a CVD-deposited MoS_2 film exhibits a heightened density of

6 defects.[32–35]

7 *B.   Band alignment*

8   In addition to the previously mentioned interface chemistry, the band alignments

9 between the metal and MoS_2 substrates can be determined by analyzing the shifts of the

10 Mo $3d$ spectra following metal deposition.[31] The shifts of Mo $3d$ peaks are based on the

11 binding energies of the MoS_2 state before and after metal depositions under UHV

12 conditions, see supplementary material, Table S1, and Figure S2. The electron affinities

13 (χ) and ionization energy (E_i) which is related to the work function of substrates and are

14 calculated from the secondary electron (SE) cutoff and valence band spectra measured by

15 XPS. The E_i and χ of MoS_2 bulk used in this study are consistent with those employed by

16 Wang et al.[31] Spectra with detailed measurement values are available in supplementary

17 material.

18   Figure 3 shows the band alignment study of bulk and 1-L MoS_2 before and after

19 metallization. Since in the UHV ambient, where spurious residual water or carbon species

20 were minimal, the reproducibility of Fermi levels, measured from the valence band, SE

21 cutoff, and core level shifting, should be expected. Considerable differences in the

22 positions of E_F are observed depending upon the MoS_2 substrate for Sn metal contacts. The

23 E_F of Sn/1L-MoS_2 film after metal depositions is located close to the original E_F's of the

1   as-received 1L-MoS$_2$ films before metal depositions. This finding indicates that the gap

2   states induced by pre-existing defects of 1L-MoS$_2$ films probably saturated the charge

3   transfer

5

6   FIG. 3. Band alignment of contact metal/MoS$_2$ systems before and after metal depositions

7   under UHV conditions.

8

9   during Sn/1L-MoS$_2$ interface formation,[36] which ultimately led to E_F pinning. For the MoS$_2$

10   bulk sample with a lower defect density, the E_F has moved near the conduction band

11   minima (CBM) of bulk MoS$_2$ which is likely induced by the work function of Sn metal[37]

12   after metal deposition as anticipated. With a low Schottky barrier height, Sn is able to

13   nearly form an ohmic contact if active defects can be reduced to a reasonable amount,

1 $(\leq 10^{11}/cm^2)$.[38–40] The results indicate the advantages of using low-work function metal for

2 n-type contact formation at the Sn/MoS$_2$ bulk interfaces after Sn deposition. This

3 additionally clarifies the low contact resistance of the exfoliated MoS$_2$ monolayer with Sn

4 contacts reported in the reference.[14]

C.   Thermal stability

1.   Sn/MoS$_2$ bulk crystal interface

7   The interface chemistry of the Sn/MoS$_2$ bulk crystal after Sn deposition and

8 following the in-situ annealing (UHV) process at different temperatures is illustrated in

9 Figure 4. After Sn deposition, only the MoS$_2$ bulk bonding state was detected in both Mo

10 3d and S 2p at the Sn/bulk MoS$_2$ interface, and after subsequent UHV annealing, no

11 additional state appeared. The reaction between Sn and MoS$_2$ stayed below the detection

12 limit until 300˚C annealing (Figure 4 (a)). However, with increasing temperature (above

13 100 ˚C), Sn starts to sublimate from the sample surface, and the intensity of metallic Sn^0

14 in Sn 3d decreases (Figure 4 (b)). This finding is consistent with the high vapor pressure

15 and low melting point of Sn (T_m=232˚C).[41] Upon annealing above 300 ˚C, most Sn metal

16 desorbs from the interface. Due to only vdW interactions between Sn and bulk MoS$_2$ and

17 no capping layer on top, Sn readily detaches from the substrate surface through

18 annealing.

19   Though no interface reaction is observed up to 300 ˚C, above this temperature, Sn

20 likely initiated a reaction with the bulk MoS$_2$. The metallic Mo 3d feature (Figure 4(a)

21 "Mo^0") appeared after 400 ˚C annealing, denoting the reduction process of MoS$_2$. The

22 sub-stoichiometric state (MoS$_x$) stays below the detection limit throughout the annealing.

1 Nevertheless, the presence of metallic Mo^0 at the Sn/bulk MoS_2 interface indicates that at

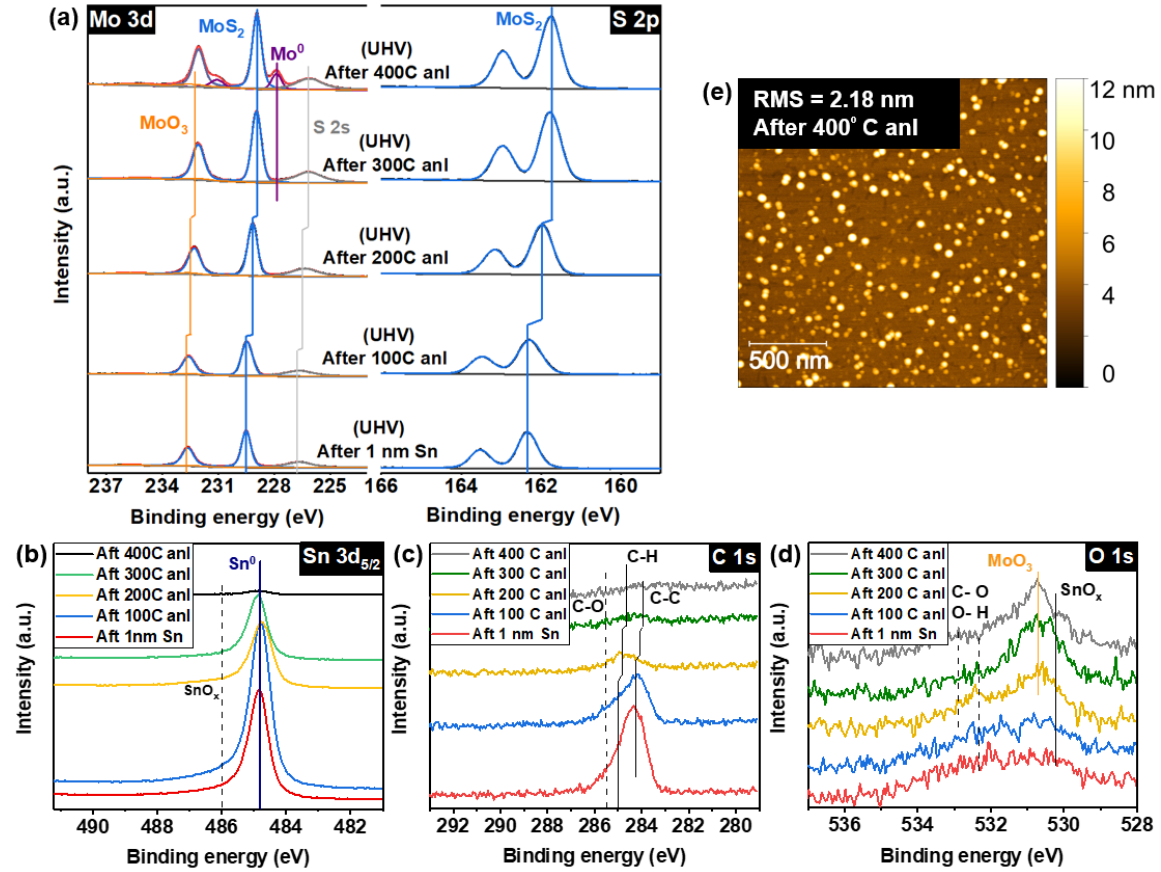2 a higher temperature (300-400 ˚C). some Sn in the form of Sn-S sublimates from the

3

4

5 FIG. 4. (a) Mo $3d$ and S $2p$, (b) Sn $3d5/2$, (c) C $1s$ and (d) O $1s$ spectra of bulk MoS_2

6 sample after Sn depositions and after sequential thermal annealing under UHV condition,

7 (e) Ex-situ AFM image of MoS_2 bulk crystal surface after 400ºC annealing reveals very

8 few islands compared to the surface before annealing.

9

10 interface. The small quantity of SnO_x detected after metallization remained relatively

11 constant throughout the annealing process. (Figure 4 (b)). The adventitious carbon

12 concentration started to reduce around 200˚ C and went down close to the XPS detection

15

1 limit after 300 $^\circ$C (Figure 5 (d)) consistent with the desorption of weakly bound species.

2 In addition to the interface chemistry, charge transfer causes a downward shift of the core

3 levels (Mo 3d and S 2p) in BE with increasing annealing temperature. (Figure 4 (a)) and

4 move them back to their previous BE before Sn deposition.

5   AFM analysis after 400 $^\circ$C annealing shows very few small islands (Figure 4 (e))

6 compared to post metallization AFM image (Figure 1 (f)). As Sn undergoes annealing at

7 temperatures higher than its T_m, Sn sublimates, and the agglomerated Sn islands

8 exhibited after metallization resulted in a reduction in their size and gradually left the

9 MoS$_2$ surface exposed. From XPS analysis after 400 $^\circ$C, we observed an extremely low

10 Sn concentration survives which is likely leaving regions of exposed substrate visible in

11 the AFM image. The XPS spectrum also shows metallic Mo features as MoS$_2$ is reduced

12 above 300 $^\circ$C. Therefore, most of the tiny islands observed in the AFM image indicate a

13 composition of metallic Mo. Additionally, the MoS$_2$ bulk surface morphology shows

14 increased surface roughness after annealing probably due to the presence of Mo islands.

15

16 *2.   Sn/1L-MoS$_2$/SiO$_2$/Si interfaces*

17   The interface chemistry of Sn/1L-MoS$_2$/SiO$_2$/Si stack after Sn deposition and

18 after in-situ annealing in UHV at different temperatures is illustrated in Figure 5. After 1

19 nm Sn deposition in UHV, the previously observed reduction reaction product in the Mo

20 3d and S 2p spectra (cf. Figure 3 (a)) indicated the Sn reduction of 1L-MoS$_2$ film. Now

21 through thermal annealing, we can illustrate the progression of the reaction species and

22 sub-stoichiometric MoS$_x$ state.

1   As the annealing temperature increases, the intensity of the MoS_2 in Mo $3d$ and S

2   $2p$ spectra enhances. In contrast, the amount of reaction products and the intensity of

3   metallic Sn^0 in Sn $3d$ remain almost unchanged (Figure 5(a) and (e)) up to 200 °C. This is

4   probably due to the small cluster formation by Sn. Above 200 °C, the reaction at the Sn/

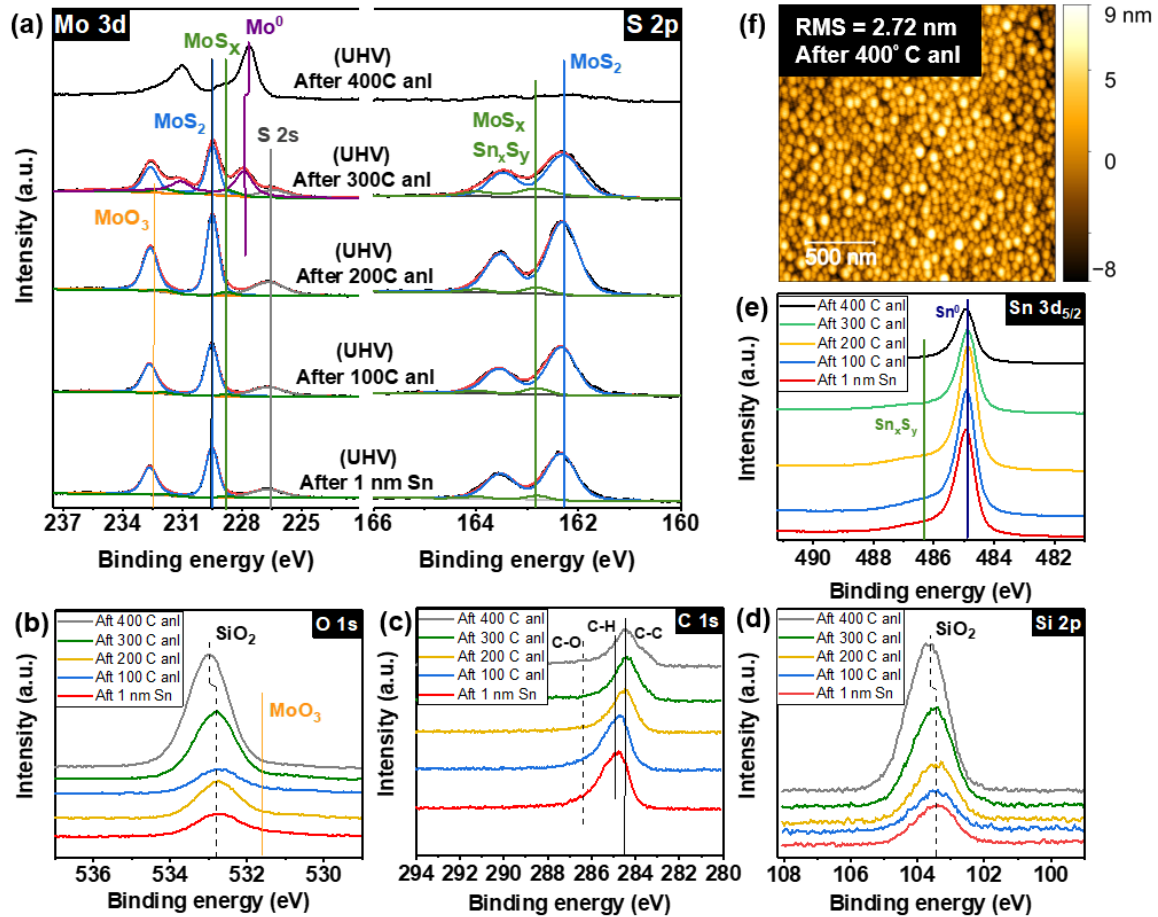5   1L-MoS_2 interface is elevated and at 300 °C excessive reduction by Sn metal of

6

8   FIG. 5. (a) Mo $3d$ and S $2p$, (b) O $1s$, (c) C $1s$, (d) Si $2p$, and (e) Sn $3d_{5/2}$ core level in-situ

9   spectra of Sn/1L MoS_2 interface showing thermal stability after subsequent UHV

10   annealing, (f) Ex-situ AFM image of the monolayer MoS_2 after 400°C annealing in UHV

11   conditions showing increasing roughness after thermal annealing.

12   .

1 monolayer MoS_2 is identified by the appearance of metallic Mo^0. In addition, the

2 intensity of the MoS_2 peak in Mo $3d$ and S $2p$ spectra decreased. This finding highlights

3 the Sn reaction with the CVD $1L-MoS_2$ film and subsequent evaporation from the

4 interface, which was observed in small amounts for the Sn/ bulk MoS_2 interface after

5 annealing at 400 °C. This reduction phenomenon at the Sn/ 1L MoS_2 interface is

6 exaggerated after annealing at 400 °C, resulting in the S $2p$ intensity nearing the detection

7 limit and a substantial portion of MoS_2 converting to metallic Mo^0. However, compared

8 to the bulk substrate (Figure 4(b)), a noticeable amount of Sn remained at the interface

9 (Figure 5 (e)). The covalent bonding at the interface between Sn and monolayer MoS_2 is

10 probably the underlying cause. There is no shifting in the core level of Mo $3d$ and S $2p$

11 after Sn deposition and subsequent annealing. As discussed above, surface defects are

12 likely the cause of such E_F pinning effects.

13 The peaks of SiO_2 in both O $1s$ and Si $2p$ spectra do not shift after annealing up to

14 300°C within the binding energy resolution limits (Figure 5 (b) and (d)). This outcome

15 indicates weak bonding between the $1L-MoS_2$ film and the SiO_2 substrate. However, after

16 annealing at 400 °C, the peaks corresponding to SiO_2 bonding in both O $1s$ and Si $2p$

17 spectra shift to higher binding energies. Between 300 °C and 400 °C, Sn sublimated from

18 the surface in the form of Sn_xS_y, leading to excessive reduction and degradation of the

19 $1L-MoS_2$ film. As a result, a significant amount of metallic Mo and a small quantity of

20 Sn_xS_y reaction products emerged at the $1L-MoS_2/SiO_2$ interface. This most likely changes

21 the band offsets of the monolayer MoS_2/SiO_2 interface as possible charge transfer is

22 expected when a CVD-grown MoS_2/SiO_2 interface is formed.[42] The removal of S by Sn

metal, away from the $1L\text{-}MoS_2/SiO_2$ interface, could also contribute to the shifts of the

SiO_2 orbital states to higher binding energies in the O $1s$ and Si $2p$ spectra.

Previously in the interface chemistry section, we observed that the interfacial

reaction between the $1L\text{-}MoS_2$ film and the SiO_2 substrate is below the detection limit of

XPS for the control sample before Sn deposition (Figure 2 (e)). Moreover, since CVD

$1L\text{-}MoS_2$ film is typically deposited on the SiO_2/Si wafer at ~ 800 °C, [43] a temperature

exceeding 400 °C during the annealing process in this work, no additional reaction is

anticipated between monolayer MoS_2 and SiO_2. Therefore, it is reasonable to speculate

that the Sn reduction reaction of $1L\text{-}MoS_2$ could induce substantial defects (S vacancies)

at the $1L\text{-}MoS_2/SiO_2$ interface, and as the MoS_2 reduction is enhanced above 300 °C, the

core level of Si $2p$ shifted to a higher BE.

AFM analysis of the $1L$ MoS_2 surface shows higher roughness values compared

to the surface before annealing (Figure 2 (g) and Figure 5 (f)). Based on XPS analysis,

the significant reduction in MoS_2 states after annealing at 400 °C, with only a few percent

of sulfur remaining, suggests that most of the surface area in the AFM image is likely

covered with metallic Sn and Mo islands. This observation accounts for the combined

desorption of Sn and S as Sn_xS_γ reaction products. As both the Mo^0 and Sn metal features

dominate the surface morphology, an increase in surface roughness was observed after

annealing at 400 °C.

IV. SUMMARY AND CONCLUSIONS

In conclusion, Sn contacts' interface chemistry and band alignment on MoS_2

substrates are thoroughly studied via in-situ XPS and ex-situ AFM analysis. Sn forms a

vdW contact interface with the bulk substrate and a covalent-type interface with the monolayer substrate. The Sn aligns the E_F of bulk MoS_2 close to the CBM with a minimum barrier height while E_F pinning is observed in $Sn/1L-MoS_2$ interface due to intrinsic defects in CVD-grown MoS_2. In addition, the thermal stability of an uncapped Sn metal contact is examined on both substrates up to 400 °C. Although the Sn/bulk MoS_2 interface reaction is below the detection limit of XPS until 300 °C, excessive sublimation of Sn from the surface left a bare bulk surface after annealing above 300 °C. The reaction products at $Sn/1L$ MoS_2 from the reduction of monolayer substrate increased gradually with subsequent annealing process. Above 300 °C the $Sn/1L$ MoS_2 indicated a highly reactive interface and consequently, after 400 °C Sn substantially reduced the MoS_2 surface and formed metallic Mo. Both substrates got reduced by Sn when the temperature exceeded 300°C, and the excessive desorption and reduction of the S $2p$ signal suggest combined evaporation of Sn_xS_y from the surfaces, particularly for monolayer MoS_2.

SUPPLEMENTAL MATERIAL

The following files are available free of charge.

The deposition/analysis process flow, core level BE and FWHMs of the bulk MoS_2 substrates with the Sn contact interface, and the band alignment extraction procedure are available.

AUTHOR DECLARATIONS

Conflict of Interest: The authors have no conflicts to disclose.

Author Contributions: Joy Roy: Conceptualization (lead); data curation (lead); methodology (lead); writing – original draft (lead); formal analysis (lead); writing – review and editing (equal). Seong Yeol Kim: Methodology (equal); formal analysis (equal); writing – review and editing (equal). Robert M. Wallace: Conceptualization (equal); funding acquisition (lead); methodology (equal); resources (lead); supervision (lead); writing – review and editing (equal).

DATA AVAILABILITY

The data that support the findings of this study are available within the article and its supplementary material as figures. The data that support the findings of this study are also available from the corresponding author upon reasonable request.

REFERENCES

[1] R. Ganatra, and Q. Zhang, ACS Nano **8**, 4074 (2014).

[2] A. Penumatcha, K.P. O'Brien, K. Maxey, W. Mortelmans, R. Steinhardt, S. Dutta, C.J. Dorow, C.H. Naylor A., K. Kitamura, T. Zhong, T. Tronic, P. Buragohain, C. Rogan, C.-C. Lin, M. Kavrik, J. Lux, A. Oni, A. Vyatskikh, S. Lee, N. Arefin, P. Fischer, S. Clenndenning, M. Radosavljevic, M. Metz, and U. Avci, in *2023 International Electron Devices Meeting* (IEEE, 2023), pp. 1–4.

[3] Z. Yin, H. Li, H. Li, L. Jiang, Y. Shi, Y. Sun, G. Lu, Q. Zhang, X. Chen, and H. Zhang, ACS Nano **6**, 74 (2012).

[4] H. Li, J. Wu, Z. Yin, and H. Zhang, Acc. Chem. Res. **47**, 1067 (2014).

[5] A.-S. Chou, C.-C. Cheng, S.-L. Liew, P.-H. Ho, S.-Y. Wang, Y.-C. Chang, C.-K. Chang, Y.-C. Su, Z.-D. Huang, F.-Y. Fu, C.-F. Hsu, Y.-Y. Chung, W.-H. Chang, L.-J. Li, and C.-I. Wu, IEEE Electron Device Lett. **42**, 272 (2021).

[6] G. Arutchelvan, Q. Smets, D. Verreck, Z. Ahmed, A. Gaur, S. Sutar, J. Jussot, B. Groven, M. Heyns, D. Lin, I. Asselberghs, and I. Radu, Sci. Rep. **11**, 6610 (2021).

[7] S. Wang, X. Liu, and P. Zhou, Adv. Mater. **34**, 2106886 (2022).

[8] J. Lin, S. Monaghan, N. Sakhuja, F. Gity, R.K. Jha, E.M. Coleman, J. Connolly, C.P. Cullen, L.A. Walsh, T. Mannarino, M. Schmidt, B. Sheehan, G.S. Duesberg, N. McEvoy, N. Bhat, P.K. Hurley, I.M. Povey, and S. Bhattacharjee, 2D Mater. **8**, 025008 (2020).

[9] D. Akinwande, C. Huyghebaert, C.-H. Wang, M.I. Serna, S. Goossens, L.-J. Li, H.-S.P. Wong, and F.H.L. Koppens, Nature **573**, 507 (2019).

[10] A. Rai, H.C.P. Movva, A. Roy, D. Taneja, S. Chowdhury, and S.K. Banerjee, Crystals **8**, 316 (2018).

[11] Y. Wang, and M. Chhowalla, Nat. Rev. Phys. **4**, 101 (2022).

[12] J. Kang, W. Liu, and K. Banerjee, Appl. Phys. Lett. **104**, 93106 (2014).

[13] H. Lu, Z. Liu, X. Yan, D. Li, L. Parent, and H. Tian, Sci. Rep. **6**, 24366 (2016).

[14] A. Kumar, K. Schauble, K.M. Neilson, A. Tang, P. Ramesh, H.-S.P. Wong, E. Pop, and K. Saraswat, in *2021 International Electron Devices Meeting* (IEEE, 2021), p. 7.3.1-7.3.4.

[15] P.-C. Shen, C. Su, Y. Lin, A.-S. Chou, C.-C. Cheng, J.-H. Park, M.-H. Chiu, A.-Y. Lu, H.-L. Tang, M.M. Tavakoli, G. Pitner, X. Ji, Z. Cai, N. Mao, J. Wang, V. Tung, J. Li, J. Bokor, A. Zettl, C.-I. Wu, T. Palacios, L.-J. Li, and J. Kong, Nature **593**, 211 (2021).

[16] A.-S. Chou, T. Wu, C.-C. Cheng, S.-S. Zhan, I.-C. Ni, S.-Y. Wang, Y.-C. Chang, S.-L. Liew, E. Chen, W.-H. Chang, C.-I. Wu, J. Cai, H.-S.P. Wong, and H. Wang, in *2021 IEEE International Electron Devices Meeting* (IEEE, 2021), p. 7.2.1-7.2.4.

[17] Y. Wang, J.C. Kim, R.J. Wu, J. Martinez, X. Song, J. Yang, F. Zhao, A. Mkhoyan, H.Y. Jeong, and M. Chhowalla, Nature **568**, 70 (2019).

[18] HQ Graphene. www.hqgraphene.com (accessed 12 June 2024)

[19] 2dlayer. https://2dlayer.com/ (accessed 12 June 2024).

[20] C.M. Smyth, R. Addou, C.L. Hinkle, and R.M. Wallace, J. Phys. Chem. C **124**, 14550 (2020).

[21] XPS Oasis. https://xpsoasis.org/ (accessed 12 June 2024).

[22] Gwyddion. http://gwyddion.net/ (accessed 12 June 2024).

[23] X. Wang, C.R. Cormier, A. Khosravi, C.M. Smyth, J.R. Shallenberger, R. Addou, and R.M. Wallace, Surf. Sci. Spectra **27**, 014019 (2020).

[24] W.M. Haynes, *CRC Handbook of Chemistry and Physics* (CRC Press, Boca Raton, 2016).

[25] H. Mo, X. Zhang, Y. Liu, P. Kang, H. Nan, X. Gu, K.K. Ostrikov, and S. Xiao, ACS Appl. Mater. Interfaces **11**, 39077 (2019).

[26] T.B. Massalski, H. Okamoto, Pr. Subramanian, L. Kacprzak, and W.W. Scott, *Binary Alloy Phase Diagrams* (ASM International, Materials Park, OH, 1986).

[27] R. Szoszkiewicz, Materials **14**, 5979 (2021).

[28] R. Addou, and R.M. Wallace, J. Electron Spectros. Relat. Phenomena **231**, 94 (2019).

[29] A.F. Lee, and R.M. Lambert, Phys. Rev. B **58**, 4156 (1998).

[30] J.F. Moulder, W.F. Stickle, W.M. Sobol, and K.D. Bomben, *Handbook of X-Ray Photoelectron Spectroscopy*, (PHI Division, Perkin-Elmer Corporation, 1992).

[31] X. Wang, S.Y. Kim, and R.M. Wallace, ACS Appl. Mater. Interfaces **13**, 15802 (2021).

[32] J. Hong, Z. Hu, M. Probert, K. Li, D. Lv, X. Yang, L. Gu, N. Mao, Q. Feng, L. Xie, J. Zhang, D. Wu, Z. Zhang, C. Jin, W. Ji, X. Zhang, J. Yuan, and Z. Zhang, Nat Commun. **6**, 6293 (2015).

[33] C. Durand, X. Zhang, J. Fowlkes, S. Najmaei, J. Lou, and A.-P. Li, J. Vac. Sci. Technol., B **33**, 02B110 (2015).

[34] D.J. Trainer, J. Nieminen, F. Bobba, B. Wang, X. Xi, A. Bansil, and M. Iavarone, npj 2D Mater. Appl. **6**, 1 (2022).

[35] X. Fan, R. Siris, O. Hartwig, G.S. Duesberg, and F. Niklaus, ACS Appl. Mater. Interfaces **12**, 34049 (2020).

[36] Y.Y. Illarionov, A.G. Banshchikov, D.K. Polyushkin, S. Wachter, T. Knobloch, M. Thesberg, L. Mennel, M. Paur, M. Stöger-Pollach, A. Steiger-Thirsfeld, M.I. Vexler, M. Waltl, N.S. Sokolov, T. Mueller, and T. Grasser, Nat. Electron. **2**, 230 (2019).

[37] M. Akbi, and A. Lefort, J. Phys. D: Appl. Phys. **31**, 1301 (1998).

[38] R. Addou, L. Colombo, and R.M. Wallace, ACS Appl. Mater. Interfaces **7**, 11921 (2015).

[39] F. Bussolotti, J. Yang, H. Kawai, C.P.Y. Wong, and K.E.J. Goh, ACS Nano **15**, 2686 (2021).

[40] S.M. Gali, A. Pershin, A. Lherbier, J.-C. Charlier, and D. Beljonne, J. Phys. Chem. C **124**, 15076 (2020).

[41] Y. Lan, and C. Huang, J. Energy Storage **54**, 105203 (2022).

1   [42] L. Su, Publication No. 3744310, (Doctoral dissertation, The University of North Carolina

2   at Charlotte, ProQuest Dissertations & Theses database, 2015)

3   [43] D. Zhou, H. Shu, C. Hu, L. Jiang, P. Liang, and X. Chen, Cryst. Growth Des. **18**, 1012

4   (2018).

5